

IN SITU HIGH TEMPERATURE HEAT FLUX SENSOR CALIBRATION

Clayton A. Pullins, Tom E. Diller*

Department of Mechanical Engineering, Virginia Tech, Blacksburg, VA 24061-0238, United States

Abstract

Recent advances in heat flux measurement have resulted in the development of a robust thermopile heat flux sensor intended for use in extreme thermal environments. The High Temperature Heat Flux Sensor (HTHFS) is capable of simultaneously measuring thermopile surface temperature and heat flux at sensor temperatures up to 1000 °C. The need for high temperature heat flux calibration of the HTHFS has resulted in the development of a new wide angle radiation calibration system, which operates with the sensor at elevated temperatures. The temperature dependence of the sensor output over the range of 100 °C to 900 °C has been successfully characterized with acceptable uncertainty limits. The calibrated HTHFS sensitivity agrees well with a theoretical sensitivity model, suggesting that the primary cause for the sensor's output temperature dependence is due to the change in thermal conductivity of the sensor elements with temperature.

Nomenclature

A	area (cm ²)
D	cavity diameter (cm)
F	radiation view factor
f	correction factor applied to sensitivity calculation
g	gravitational vector
k	statistical coverage factor
l	characteristic length (cm)
L	cavity length (cm)
q	heat transfer rate (W)
q''	heat flux (W cm ⁻²)
r	radius (cm)
s	sample standard deviation
S	sensitivity to absorbed heat flux ($\mu\text{V W}^{-1} \text{cm}^2$)
Se	relative Seebeck coefficient ($\mu\text{V } ^\circ\text{C}^{-1}$)
T	temperature (°C)
u	standard uncertainty
u_c	combined standard uncertainty
u_r	uncertainty in the repeatability of the calibration
U	expanded uncertainty
V	thermoelectric voltage (μV)

Greek Letters

α	hemispherical total absorptivity
----------	----------------------------------

δ	Kronecker delta
ϵ	hemispherical total emissivity
κ	thermal conductivity (W cm ⁻¹ °C ⁻¹)
ν	number of effective degrees of freedom
σ	Stefan-Boltzmann constant (W cm ⁻² K ⁻⁴)

Subscripts

a	absorbed
avg	average
c	pertaining to the cold plate surface
cond	conduction
conv	conduction
h	pertaining to the hot plate surface
inc	incident
net	calculated net
rad	radiation
s	pertaining to the surface
sb	pertaining to the Schmidt-Boelter sensor
t	pertaining to the HTHFS
w	pertaining to the cavity wall surface

1. Introduction

Heat flux measurement is a complex process that requires careful design and implementation of both sensors and calibration systems to ensure accuracy in the measurements. Heat flux is a critical parameter in many engineering systems, such as vehicle thermal protection and propulsion systems. Direct measurement of heat flux can be accomplished with

*Research advisor. Tel.: +1 540 231 7198
Email addresses: cpullins@vt.edu (Clayton A. Pullins), tdiller@vt.edu (Tom E. Diller)

the use of a differential temperature sensor. Differential temperature sensors measure a spatial temperature gradient which is proportional to heat flux. One type of sensor, the thermopile, measures differential temperature directly using a series connection of thermocouples across a thermal resistance. Thermopile measurement principles are summarized in¹; also provided is a list of commercially available heat flux sensors. All sensors considered in this study are thermopile sensors, which are often referred to as “total” heat flux sensors because they respond to all three modes of heat transfer.

Thermopile heat flux sensors are typically grouped into two categories: flush-mounted insert gages or surface-mounted flat gages; standard test methods for both types are outlined in^{2,3}. The upper temperature limit (continuous use) for both categories of thermopile sensors is typically below 300 °C¹. Insert gages are often water cooled to maintain their temperature at acceptable levels. Often, direct measurement of heat flux is required, however, the inherent complications associated with a water cooled sensor may not be desired. For such cases, uncooled sensors capable of withstanding a given thermal environment are appropriate. The need for a heat flux sensor capable of operation at high temperatures (> 300 °C) led to the development of the High Temperature Heat Flux Sensor (HTHFS) at Virginia Tech⁴. The present paper introduces a novel method for calibrating the HTHFS and other uncooled differential heat flux sensors at elevated sensor temperatures. To the authors’ knowledge, no such system is currently in operation.

2. Virginia Tech’s High Temperature Heat Flux Sensor

The HTHFS is capable of simultaneous measurement of thermopile surface temperature and heat flux. The sensor’s upper temperature limit (continuous use) is 1000 °C. A brief description of the sensor is presented in the following sections; a more detailed description of the HTHFS design and operation is given by Gifford et al.⁴.

2.1. HTHFS Design

Unlike other thermopile sensors, the HTHFS thermocouple elements (K-type) serve as the thermal resistance of the sensor. The elements are welded together to form a durable thermopile. When heat flows through the thermopile, the sensor

Pullins

outputs a voltage, V_t , proportional to the temperature difference across the sensor’s thermal resistance:

$$V_t = NSe(T_1 - T_2) \quad (1)$$

Here N is the number of thermocouple junction pairs in the thermopile, and Se is the relative Seebeck coefficient of the thermocouple alloys. The thermopile voltage output is related to heat conduction by Fourier’s law (one-dimensional, steady-state):

$$q'' = -\kappa \frac{dT}{dx} = \kappa_t \frac{T_1 - T_2}{l_t} = \frac{\kappa_t V_t}{l_t N Se} \quad (2)$$

where l_t and κ_t are, respectively, the length (in the direction of heat flow) and thermal conductivity of the sensor’s thermal resistance layer. The HTHFS has a surface thermocouple (K-type) welded onto both the top and bottom of the thermopile. The positive (chromel) legs of the two surface thermocouples serve as the lead wires for the thermopile bulk output. The thermopile (1.0 cm × 0.5 cm × 0.32 cm) is secured in an inconel housing (2.54 cm × 1.27 cm × 0.32 cm) with set screws and cast aluminum nitride as shown in Fig. 1. Because the HTHFS is intended for in-situ measurement in hot structure testing, no active cooling mechanism is built into the sensor.

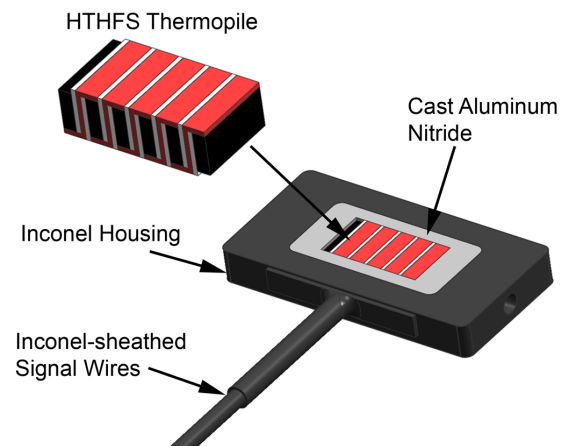


Figure 1: HTHFS secured in inconel housing.

2.2. Theoretical HTHFS Sensitivity

The HTHFS sensitivity, S_t , to an applied heat flux is defined as

$$S_t \equiv \frac{V_t}{q''} \quad (3)$$

where q'' is the average heat transfer through the sensor divided by the surface area of the sensor. Combining Eqs. 2–3, the HTHFS sensitivity can be written as

$$S_t = \frac{l_t N S_e}{\kappa_t} \quad (4)$$

The HTHFS thermopile is composed of three materials: chromel, alumel, and zirconia toughened alumina (ZTA). Assuming one-dimensional conduction and uniform temperature profiles perpendicular to the direction of heat transfer, the HTHFS composite thermal conductivity, κ_t , can be calculated with the use of an equivalent thermal circuit as described in⁵. The calculation of κ_t requires knowledge of the geometry and material properties of the sensor components.

Thermal conductivity versus temperature data was taken from⁶ for both chromel and alumel, which have nickel mass fractions of 90 % and 95 %, respectively. The ZTA ceramic is made from alumina and zirconia, with respective volume fractions of 85 % and 15 %. The zirconia is assumed to be evenly dispersed in the composite. ZTA composite thermal conductivity versus temperature was calculated using the Maxwell-Eucken method⁷ with data taken from⁸ and⁹ for alumina and zirconia, respectively. A second-order polynomial model is applied to both the chromel and alumel data in order to predict their conductivities at higher temperature than reported in⁶. The polynomial models fit the chromel and alumel data well (Fig. 2a), and are consistent with the behavior of nickel in the 500 °C to 900 °C range⁵. Figure 2a shows the thermal conductivity of HTHFS components versus temperature, as well as the calculated HTHFS composite thermal conductivity versus temperature.

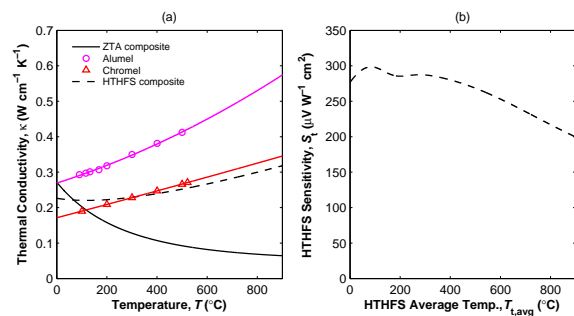


Figure 2: a) Element thermal conductivity and b) sensitivity of HTHFS thermopile.

Incorporating change in κ_t and S_e with temperature allows the prediction of the thermopile’s sensitivity versus thermopile average temperature,

Pullins

according to Eq. 4. The relative Seebeck coefficient versus temperature for K-type thermocouples is taken from¹⁰. Applying the $\kappa_t(T)$ and $S_e(T)$ trends to the theoretical sensitivity calculation results in the dashed curve shown in Fig 2b. For simplicity, the effect of thermal expansion ($L = L(T)$) on sensitivity is considered negligible. The predicted thermopile sensitivity decreases with increasing temperature above 300 °C. The strange trend in the theoretical sensitivity around 100 °C can be attributed to $S_e(T)$. A high temperature calibration system, discussed in the following section, was designed and characterized with the goal of experimentally determining HTHFS output temperature dependence.

3. High Temperature Calibration System

The primary goal of the proposed calibration system is to produce repeatable, radiative heat flux at elevated sensor temperatures, with minimal uncertainty. The system is specifically designed for high temperature sensors that are not actively cooled. The design and characterization of the system is outlined in the following sections.

3.1. Conceptual Design: Cylindrical Radiation Cavity

The cylindrical radiation cavity, shown schematically in Fig. 3, consists of two horizontal plates which are separated by a distance, L . The system confines atmospheric air in a cylindrical cavity with diameter, D , and aspect ratio, L/D . It is desired that the inner surfaces of the two horizontal plates are maintained at constant temperature under steady-state operation, where T_h and T_c are the inner surface temperatures of the hot and cold plates, respectively. The cylindrical sidewall is intended to represent an ideal reradiating surface, characterized by zero net radiation heat transfer ($q_w = 0$). Reradiating surfaces are closely represented by real surfaces that are well insulated on one side and have negligible convective heat transfer on the opposite side⁵. In an effort to combat natural convection effects inside the cavity, the system is oriented such that the hot plate is located above the cold plate, with the gravity vector pointing downward, orthogonal to the horizontal plates (Fig. 3).

Assuming radiation exchange between diffuse-gray surfaces with uniform radiosities, a simple equation for the heat transfer from the hot plate to the cold plate with the sidewall acting as a reradiating surface has the form⁵

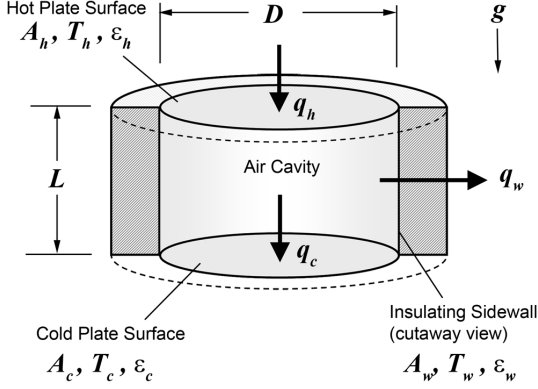


Figure 3: High temperature calibration system schematic.

$$\frac{q_h}{A_h} = q_h'' = q_c'' = \frac{\sigma(T_h^4 - T_c^4)}{\left[\frac{1-\epsilon_h}{\epsilon_h} + \frac{2}{F_{hc}+1} + \frac{1-\epsilon_c}{\epsilon_c} \right]} \quad (5)$$

where the subscripts represent the surfaces in the enclosure shown in Fig. 3: surface (h) is the hot plate inner surface, surface (c) is the cold plate inner surface, and surface (w) is the insulating sidewall inner surface, which is approximated as the reradiating surface. The net heat transfer rate through each control surface, q_s , has a direction as shown in Fig. 3. The variables T , ϵ , and A of Eq. 5 are, respectively, absolute temperature (K), emissivity, and area of the specified surface (note: $A_h = A_c$). The radiation view factor, F_{12} , is defined as the fraction of radiation leaving surface 1 that is intercepted by surface 2; from the summation of view factors, $F_{cw} = F_{hw} = 1 - F_{hc}$. The Stefan-Boltzmann constant, σ , is equal to $5.67 \times 10^{-12} \text{ W cm}^{-2} \text{ K}^{-4}$. One thing to note about Eq. 5 is that the heat transfer does not depend on the sidewall emissivity, ϵ_w , for an adiabatic sidewall.

From Eq. 5 it is apparent that, for a set temperature difference between the hot and cold plates, increasing either ϵ_c , ϵ_h , or F_{hc} increases heat flux. In the limiting case (for a given plate area) as ϵ_h , ϵ_c , and F_{hc} approach their theoretical limit of unity, the radiation exchange between the plates approaches blackbody behavior. The radiation view factor for a given cavity size is calculated as

$$F_{hc} = 1 - 2 \left(\frac{L}{D} \right)^2 \left[\sqrt{\left(\frac{D}{L} \right)^2 + 1} - 1 \right] \quad (6)$$

which approaches unity in the limit as either $D \rightarrow \infty$ or $L \rightarrow 0$.

Pullins

3.2. Physical Design

With the conceptual cavity design serving as a guideline, a prototype high temperature calibration system has been constructed and tested. The prototype consists of a hot plate and a cold plate in which heat flux sensors are flush mounted (in the center of each plate) and separated by an air cavity. The system is designed to operate with the hot plate on top (with respect to earth gravity vector) to reduce natural convection. A plate diameter of 7.62 cm was chosen to accommodate a wide range of radiation cavity diameters, while limiting the power requirement for the heater system. The sidewall, made from rigid fibrous alumina, is machined accordingly to provide the desired cavity size. For this analysis, the sidewall was machined to form a radiation cavity where $L = 1.27 \text{ cm}$ and $D = 5.08 \text{ cm}$ ($L/D = 0.25$). A resistance heater potted into the hot plate provides heat to the system, while water cooling in the cold plate provides the means of heat removal. The entire system is encased in rigid fibrous alumina insulation to limit heat loss to the surroundings. Figure 4 shows a CAD model of the calibration system with labeled components.

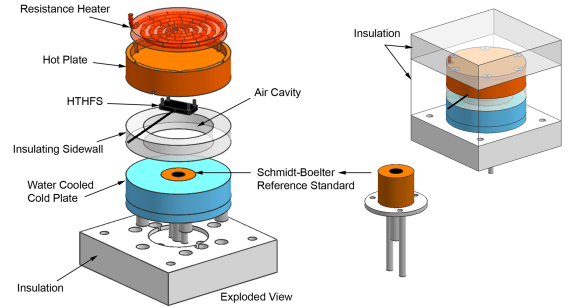


Figure 4: High temperature calibration system CAD model.

The aluminum cold plate houses a reference standard Schmidt-Boelter (SB) heat flux sensor (Medtherm model No. 64-30SB-20K) which is mounted flush with the plate surface. The SB sensor's calibration is traceable to NIST temperature and electrical standards. Both the SB sensor and the cold plate in which it is housed have internal channels for cooling water. The stainless steel hot plate houses one HTHFS which is flush mounted in the plate (Fig. 5). An inconel sheathed, flat-spiral coil heater is mechanically fastened to the backside of the hot plate with a stainless steel cap plate. Cast aluminum nitride fills the void areas between the coil and hot plate to reduce contact resistance. The hot and cold plate sandwich the insulating sidewall, forming the cylindrical air cavity in which the radiation exchange between the plates takes place.

4

The system is designed to transfer heat flux calibration from the secondary standard SB sensor to the HTHFS.

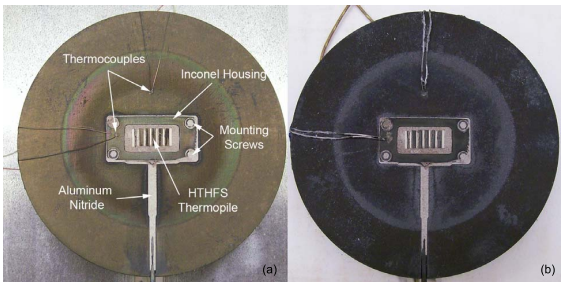


Figure 5: Stainless steel hot plate housing flush mounted HTHFS with a) initial and b) heavy surface oxidation.

3.3. Experimental Setup

Experimental characterization of the system began with comparing initial measurements from the reference standard SB sensor to the ideal solution (Eq. 5). Steady-state heat flux events were physically realized by controlling power to the resistance heater with the use of a single-phase 120 VAC variable transformer. One steady-state thermal event was produced for hot plate temperatures from 100 °C to 900 °C in steps of approximately 100 °C (nine thermal events per test). Room temperature water was circulated through the cold plate and SB sensor using a small submersible pump. Flow rates of 17 mL s⁻¹ and 14 mL s⁻¹ were maintained for the cold plate and SB sensor, respectively.

In order to characterize system performance, temperature measurements were made with K-type thermocouples at various locations inside the cavity. Cold plate temperatures were measured with a thermocouple in the SB sensor along with two thermocouples spot welded onto the surface of the cold plate. Hot plate temperatures were measured with five thermocouples: two thermocouples built into the HTHFS, one thermocouple built into the heater, and two fine wire thermocouples spot welded onto the hot plate surface (as shown in Fig. 5). The surface thermocouples are electrically connected to the plates only at the junction. In early tests, the wires were electrically isolated from the hot plate surface using ceramic sleeves. Once a heavy oxidation layer formed on the hot plate surface, the ceramic sleeves were no longer necessary to prevent electrical contact between the plate and thermocouple lead wires. Heat conduction from the thermocouple junction through the lead wires is assumed negligible, because the fine wires, routed along the

hot plate surface, are assumed to be at approximately the same temperature as the plate surface.

Temperature and heat flux signals were read into 24-bit National Instruments CompactDAQ thermocouple modules as analog differential inputs. Cold-junction temperature was compensated for each channel using on board thermistor measurements. The ± 125 mV range of the analog-to-digital converter provides significant resolution for the expected output from the heat flux sensors with a least significant bit of $0.25/2^{24} = 14.9$ nV.

The cold plate surface was painted with flat black paint to match the SB sensor face ($\epsilon_c = \epsilon_{sb} = 0.94$). The hot plate surface was left uncoated: the paint used on the cold plate has an upper temperature limit of approximately 630 °C, which is below the desired upper temperature bound for the hot plate of 900 °C. Preliminary test runs were performed over the full operating range of the system to allow the hot plate surface to oxidize (Fig. 5), increasing its emissivity.

3.4. System Characterization

To transfer calibration from the reference standard to the HTHFS, the heat flux experienced by each sensor must be well known (ideally equal). Although the ideal solution (Eq. 5) provides insight to system operation, a more detailed analysis of system operation is required to characterize the heat flux experienced by each sensor. Small discrepancies in the heat flux experienced by each sensor is expected due to the inherent differences in the sensors' designs. The effect of each sensor's geometry and intrusiveness on the heat flux transfer calibration was considered. Unlike the assumption made in Eq. 5, the surface radiosities are not exactly uniform over each plate. Instead, due to the geometrical view factor, the heat flux is highest at the center of the plates. Because of the nonlinear heat flux distribution on each plate, the average heat flux experienced by each sensor will not be exactly the same if the sensing areas are different.

The presence of the sensors in the measurement environment has a small effect on the temperature profile on each plate. Preliminary tests revealed that, although the HTHFS and stainless steel plate thermal properties were well matched, the contact resistance between the plate and sensor results in some plate surface temperature discontinuity. At high operating temperatures, the difference in measured plate surface temperature and HTHFS thermopile surface temperature was as high as 30 °C. For these reasons, it is expected that the heat flux experienced by each sensor is slightly different. To

account for such effects, an analytical model was developed, using measured temperatures to calculate the heat flux distribution on each surface of the cavity. The following sections outline the methods used to correct for the small heat flux discrepancies between the two sensors.

3.4.1. Analytical Model

An analytical model was used to characterize the heat flux distribution on the hot and cold plate surfaces. Experimentally measured surface temperatures serve as inputs to the analytical model. The model assumes heat is transferred through air by conduction with no convection, and that the air does not participate in the radiation exchange. Because the top-heated orientation dictates stable stratification of the air within the cylindrical cavity, it is assumed that convection exchange is negligible. Numerical and experimental results in^{11,12} indicate that heat transfer through air in the top-heated cylindrical cavity occurs by conduction only, although inclination of the cavity (cavity centerline axis with respect to gravity vector) can cause weak circulation in the air.

As a conservative approach, correlations from^{11,12} have been used to estimate the potential convection error caused by inclination of the cavity. For an inclination angle of 10° , the maximum predicted augmentation of heat transfer by convection is less than 5 % of the calculated conduction heat transfer for all test conditions. For each steady-state thermal event, a worst-case estimate of the convection error at each surface is $q''_{s,\text{conv}} = 0.05 \times q''_{s,\text{cond}}$. The effects of convection error on the heat flux calibration are examined in §3.6.

Considering radiation and conduction exchange within the cavity (neglecting convection), the net heat flux from each surface, $q''_{s,\text{net}}$, is calculated as

$$q''_{s,\text{net}} = q''_{s,\text{cond}} + q''_{s,\text{rad}} \quad (7)$$

where $q''_{s,\text{cond}}$, the conduction component of heat flux out of the surface, and $q''_{s,\text{rad}}$, the radiation component of heat flux out of the surface, are considered uncoupled. Assuming one-dimensional conduction through the air cavity,

$$q''_{s,\text{cond}} = -\kappa_{\text{air}} \frac{dT}{dx} = \kappa_{\text{air}} \frac{T_{h,\text{avg}} - T_{c,\text{avg}}}{L} \quad (8)$$

with κ_{air} taken at the film temperature. The temperature gradient is simply the difference in the average measured surface temperature of the hot and cold plate divided by the cavity length, L .

Pullins

Assuming diffuse-gray radiation exchange between cavity surfaces with uniform radiosities, a general system of equations relating radiative heat flux, $q''_{j,\text{rad}}$, and surface temperature, T_j , for the i th surface is¹³

$$\sum_{j=1}^N \left(\frac{\delta_{ij}}{\epsilon_j} - F_{ij} \frac{1 - \epsilon_j}{\epsilon_j} \right) q''_{j,\text{rad}} = \sum_{j=1}^N (\delta_{ij} - F_{ij}) \sigma T_j^4 \quad (9)$$

where, corresponding to a specific surface, $i = 1, 2, \dots, N$. Also, $\delta_{ij} = 1$ when $i = j$ and is zero otherwise. In the case of a three-surface enclosure with an adiabatic sidewall, Eq. 9 is equivalent to Eq. 5. Higher accuracy in the calculated heat flux distribution may be obtained with Eq. 9 compared to Eq. 5 by breaking the each cavity surface into discrete sections of uniform temperature and radiosity.

Application of Eq. 9 to the present experimental setup, creates one equation for each surface. The hot and cold plates are each broken into three distinct surfaces: one central disk of radius r_s representing the heat flux sensing area, and two surrounding rings. The ring immediately surrounding the sensing area represents the sensor body or housing, while the outermost ring represents the plate in which the sensor is mounted. Surface temperature measurements in each section serve as inputs to the load vector (right-hand side of Eq. 9). The adiabatic sidewall is broken into five distinct ring sections, all of equal length ($L/5$). A sensitivity analysis revealed that increasing the number of sidewall sections past five has negligible effect on the calculated hot and cold plate radiosities. Because the sidewall sections are considered adiabatic ($q''_{\text{w}} = 0$), a value of 0 W cm^{-2} is input into the degree-of-freedom vector ($q''_{j,\text{rad}}$ of Eq. 9) for each sidewall section, leaving $N = 11$ equations for the $N = 11$ unknowns.

Solution of the matrix equations yields the unknown plate surface heat fluxes and sidewall radiosities. The net heat flux over each sensing area is then calculated from Eq. 7. It is important to note that for Eqs. 7-9, q'' is the net heat flux out of the surface (convention for heat flow direction). As with Eq. 5, Eq. 9 assumes that the air is perfectly translucent and there is negligible convection exchange within the cavity.

3.4.2. Parameter Estimation: Hot Surface Emissivity

Solving the radiosity matrix equations requires knowledge of the emissivity of each surface in the cavity other than the adiabatic sidewall. The cold

plate surface and SB sensor surface are coated with flat black paint with an emissivity of $\epsilon_c = \epsilon_{sb} = 0.94$. Unlike the cold surfaces, the hot surfaces (HTHFS and hot plate) are not coated with paint. Instead, they were left uncoated and allowed to oxidize over a series of heating cycles (Fig. 5). Heavily oxidized stainless steel and inconel can have surface emissivities in the range of 0.6 to 0.9^{5,13}. In order to determine the appropriate value for the unknown emissivities, a parameter estimation scheme was developed which utilizes experimental temperature and heat flux measurements. For simplicity, the HTHFS surface emissivity was assumed to be the same as the stainless steel hot plate surface emissivity. This assumption is reasonable because all materials (other than the small amount of ceramic in the HTHFS) in the hot plate and HTHFS are nickel alloys of similar composition. It is also assumed that the surface emissivity is constant, ignoring any spectral or surface temperature dependence.

As described in §3.3, each test run consists of nine steady-state thermal events. After each test run, the radiosity matrix equations are solved in a loop with values of the hot surface emissivity, $\epsilon_t = \epsilon_h$ ranging from 0.01 to 0.99, serving as the loop parameter. For each value of ϵ_h , a sum of squares function, X , is calculated as

$$X(\epsilon_h) = \sum_{i=1}^9 (q''_{sb,a}(i) - q''_{sb,net}(\epsilon_h, i))^2 \quad (10)$$

where $i = 1, 2, \dots, 9$ represents the thermal event number, $q''_{sb,a}$ is the absorbed heat flux measured by the reference standard SB sensor, and $q''_{sb,net}$ is the cold sensor heat flux calculated using Eqs. 7-9. The best estimate for ϵ_h is the one which minimizes $X(\epsilon_h)$. The use of this sum of squares function for the parameter estimation scheme ensures that the predicted heat flux (cold sensor) matches the measured heat flux (SB reference standard sensor).

Because ϵ_h can only have a value from 0 to 1, the parameter estimation loop does not need any convergence criteria to arrive at the appropriate value. Instead, the best estimate for ϵ_h will correspond to the smallest value for $X(\epsilon_h)$ over the full range of possible emissivities. Several preliminary tests were performed in order to allow the hot plate and HTHFS to become heavily oxidized. After this initial oxidation phase, five tests were run. The results from these five tests are reported in this work. The mean hot plate emissivity and sample standard deviation for the five tests was found to be 0.728 and 0.005, respectively.

Pullins

The plots shown in Fig. 6, which contain data taken from one specific test, demonstrate the parameter estimation technique and the role it plays in the determination of the heat flux correction factor, f , discussed in the following section. Figure 6a shows the sum of squares function versus hot plate emissivity; the minimum value of this function corresponds to the best estimate for ϵ_h . Figure 6b shows measured (SB sensor) and modeled heat flux (magnitude) versus hot plate temperature for the test. The cold and hot sensor predicted heat flux is calculated using the estimated parameter (ϵ_h) and measured surface temperatures applied to Eqs. 7-9.

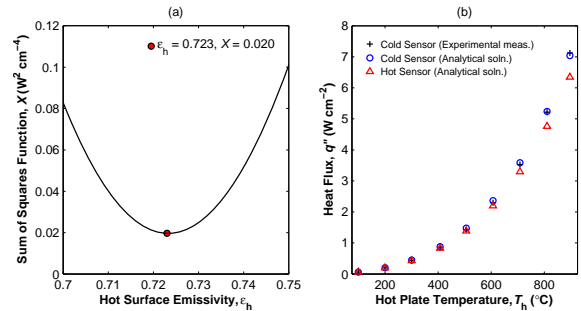


Figure 6: a) Emissivity parameter estimation and b) SB heat flux comparison.

As shown in Fig. 6b, the calculated cold sensor heat flux matches well with the measured heat flux (SB sensor). Because no noticeable trend in the difference between the predicted and measured heat flux is observed, these results appear to support the assumption that the hot plate emissivity is best estimated as a constant value for this experiment. Also shown in Fig. 6b is the predicted hot sensor heat flux, which deviates slightly from the cold sensor heat flux as the temperature of the hot plate increases. The trend in the heat flux discrepancy is due to the temperature discontinuity across the hot plate surface caused by the presence of the HTHFS. Because the temperature of the HTHFS is slightly lower than the surrounding hot plate (§3.3), the cold sensor receives more heat than that leaving the hot sensor. The effect is more profound in the high temperature range, because the radiative heat flux is proportional to the absolute temperature raised to the fourth power.

3.4.3. Heat Flux Correction Factor

To account for the predicted difference in heat flux experienced by each sensor, a correction factor, f , can be calculated for each steady-state thermal event of a specific test as

$$f = q''_{\text{sb,net}}/q''_{\text{t,net}} \quad (11)$$

where $q''_{\text{sb,net}}$ and $q''_{\text{t,net}}$, the SB and HTHFS predicted heat flux (Fig. 6), respectively, are calculated using Eqs. 7-9. The correction factor is then used in the calculation of the HTHFS sensitivity, described in the following section. Calculated correction factors for the data shown in Fig. 6 are listed in Table 1; also listed are the calculated heat fluxes used to determine f . The largest correction used in the heat flux calibration is 10 % ($f = 1.1$).

Table 1: Calculated correction factor, f , for a sample test.

$T_h /$ (°C)	$q''_{\text{sb,net}} /$ (W cm ⁻²)	$q''_{\text{t,net}} /$ (W cm ⁻²)	f
104	0.065	0.063	1.031
209	0.219	0.212	1.034
311	0.487	0.467	1.042
414	0.917	0.868	1.057
515	1.554	1.453	1.070
616	2.473	2.293	1.078
722	3.810	3.498	1.089
819	5.457	4.969	1.098
900	7.198	6.519	1.104

3.5. Calibration Results

The heat flux through each sensor's surface can be equated according to

$$q''_{\text{sb,a}} = q''_{\text{t,a}} \cdot f \quad (12)$$

where $q''_{\text{sb,a}}$ and $q''_{\text{t,a}}$ are the SB and HTHFS measured absorbed heat flux, respectively, and f is calculated for every steady-state thermal event using the analytical model. In this fashion, the SB sensor's calibration can be transferred to the HTHFS. Note, in Eq. 12 and in Fig. 6b the heat flux direction is not represented; the HTHFS thermopile is insensitive to direction, and therefore only the heat flux magnitude is presented for simplicity. The HTHFS sensitivity to absorbed heat flux is determined from

$$S_{\text{t,a}} = \frac{V_t}{q''_{\text{t,a}}} \quad (13)$$

where V_t is the HTHFS voltage output. Combining Eqs. 12–13, the HTHFS sensitivity to absorbed heat flux is

$$S_{\text{t,a}} = \frac{V_t}{V_{\text{sb}}} S_{\text{sb,a}} \cdot f \quad (14)$$

where $S_{\text{sb,a}}$ is the calibrated Schmidt-Boelter sensitivity (to absorbed heat flux) provided by the manufacturer, and the sensor output ratio, V_t/V_{sb} , is

Pullins

directly measured. If desired, the sensitivity of the HTHFS to incident radiation can be determined from

$$S_{\text{t,inc}} = \alpha_t S_{\text{t,a}} = \epsilon_t S_{\text{t,a}}, \quad (15)$$

assuming diffuse-gray radiation exchange ($\alpha = \epsilon$). Calibration results from five tests are shown in Fig. 7.

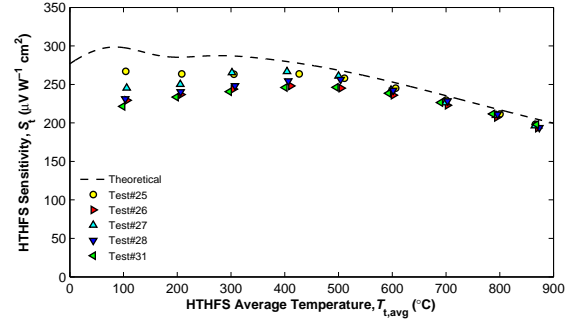


Figure 7: HTHFS calibrated sensitivity versus sensor temperature.

The theoretical sensitivity (§2.2) is plotted for comparison with experimental results. The calibrated sensitivity follows a similar trend as the theoretical sensitivity with a slightly lower magnitude over the entire temperature range, suggesting that the thermal conductivity of the thermopile is slightly higher than predicted, especially in the low temperature range. The slope in the calibrated sensitivity from 400 °C to 900 °C agrees very well with prediction. The uncertainty in the calibration results appears to be greater in the lower temperature range. A closer examination of the propagation of uncertainty in the experiment is presented in the following section.

3.6. Uncertainty Analysis

Each quantity, x_i , used to determine the HTHFS sensitivity has an associated standard uncertainty, $u(x_i)$. The combined standard uncertainty in the resulting HTHFS sensitivity, $u_c(S_{\text{t,a}})$, is determined according to¹⁴ from

$$u_c(S_{\text{t,a}}) = \sqrt{\sum_{i=1}^4 \left(\frac{\partial S_{\text{t,a}}}{\partial x_i} u(x_i) \right)^2 + (u_r)^2} \quad (16)$$

where $\partial S_{\text{t,a}}/\partial x_i$ are the sensitivity coefficients for each quantity on the right-hand side of Eq. 14. The uncertainty in the repeatability of the sensitivity

calibration, u_r , is taken to be the calculated standard deviation of the mean sensitivity determined from the sample of five tests reported in this work (see Fig. 7).

Standard uncertainties are determined using either Type A or Type B evaluation methods. Type A evaluation of standard uncertainty is based on statistical methods, while Type B evaluation is based on scientific judgment using all relevant information available. In the present paper, standard uncertainties have been evaluated using Type A methods wherever possible. In general, $u(x_i)$ is either conservatively estimated or it is represented by a statistically estimated standard deviation. A root-sum-squares technique is used when multiple sources contribute to the standard uncertainty in one quantity, x_i . Instead of using a coverage factor when determining $u(x_i)$, an overall coverage factor, k , for $u_c(S_{t,a})$ is taken as the Student's t multiplier for 95 % confidence and ν effective degrees of freedom. The effective degrees of freedom for the sensitivity calibration is calculated using the Welch-Satterthwaite formula¹⁴.

The correction factor, f , is calculated using experimental measurements and system properties applied to Eqs. 7-9 as described in §3.4.1. The combined standard uncertainty in f is calculated from the propagation of uncertainty in the quantities used to calculate the correction factor. Due to the complexity of Eqs. 7-9, a sequential perturbation numerical technique, outlined in¹⁵, is used to calculate $u_c(f)$. Calibration error caused by convection can affect the correction factor calculation by either introducing a small heat flux bias of equal magnitude between the two sensors, or by introducing a heat flux bias of unequal magnitude between the two sensors. Use of the sequential perturbation technique allowed for both of these possible scenarios to be considered in the calculation of $u_c(f)$.

The combined standard uncertainty in the HTHFS sensitivity calibration, $u_c(S_{t,a})$, is multiplied by the coverage factor, k , to get the expanded uncertainty, $U(S_{t,a})$. A coverage factor of $k = 2.03$ is used to provide a 95 % confidence interval about the measurement results (Student's t multiplier for $\nu = 35$). Figure 8 shows averaged results from five tests. The average calibration sensitivity is plotted with bars showing the expanded uncertainty in the result, which is approximately $\pm 7\%$ of the calibrated HTHFS sensitivity for sensor temperatures from 300 °C to 900 °C. A summary of the calibration results and associated uncertainties is provided in Table 2.

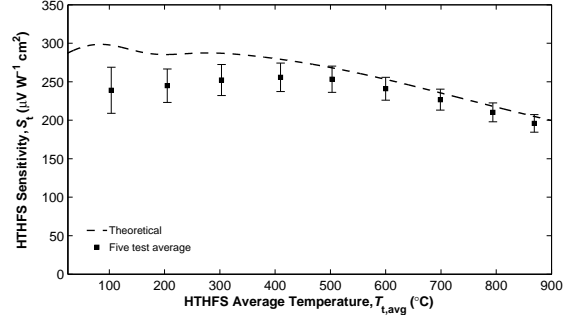


Figure 8: HTHFS calibrated sensitivity showing expanded uncertainty (95 %CI).

Table 2: Calibration results and uncertainty as a function HTHFS mean temperature, $T_{t,avg}$. Results averaged over five test sample.

$T_{t,avg}$ / (°C)	$S_{t,a}$ / ($\mu\text{V W}^{-1} \text{cm}^2$)	$U(S_{t,a})$ / ($\mu\text{V W}^{-1} \text{cm}^2$)
104	239	30
204	245	22
303	252	20
408	256	19
501	253	17
597	241	15
696	227	14
790	210	12
871	196	11

4. Discussion and Future Work

The first prototype high temperature calibration system has successfully characterized Virginia Tech's HTHFS up to 900 °C, improving the sensor's ability to accurately measure heat flux at elevated temperature. The trend in the sensor's sensitivity versus temperature agrees well with the prediction based on thermopile material properties. The bench top calibration system is both cheap and portable.

Initial results have provided useful information for future system improvement. Characterization of the system affirmed that the thermal disturbance caused by the HTHFS located in the stainless steel hot plate is small, but significant. Use of the analytical model shows how correcting for thermal disturbances may be accomplished with reasonable results. A parameter estimation scheme was developed to estimate the total hemispherical emissivity of the hot plate and hot sensor based on calibrated heat flux measurements made by the standard SB sensor. A constant value for this emissivity input into the radiosity matrix yields model results that are consistent with experimental findings.

The uncertainty analysis revealed that the major sources for uncertainty over the entire operating range of the system are in the surface emissivities used in determining f , particularly ϵ_h . Although the parameter estimation scheme chooses the most appropriate value for the hot surface emissivity, it is assumed that the emissivity is independent of spectral and surface temperature effects. High temperature coatings with well defined optical properties will be investigated for future use with the calibration system. The uncertainty analysis also showed that at low temperatures, the primary reason for the increased uncertainty in the result may be attributed to the low heat flux sensor output when compared to the uncertainty in the voltage measurement itself.

The magnitude of convection exchange inside the cavity must also be investigated. Commercial finite element software may prove useful in determining the effect of convection inside the cavity. One solution to eliminating both convection and conduction inside the cavity would be to evacuate the cavity. A cost-benefit analysis will give insight for future improvements aimed at reducing uncertainty in the calibration process.

5. Conclusions

HTHFS output temperature dependence over the range of 100 °C to 900 °C has been successfully characterized with acceptable uncertainty limits. The temperature dependency in the HTHFS output is primarily caused by change in thermal conductivity with temperature of the sensor's individual elements. The HTHFS calibrated sensitivity versus temperature has a similar trend as the theoretical sensitivity model, and suggests that the thermopile's composite thermal conductivity is slightly higher than predicted with the sensitivity model. The uncertainty in the calibration is higher in the low temperature range because the radiation heat flux is very low (same order of magnitude as conduction). Analytical modeling is necessary to account for small systematic discrepancies in heat flux experienced by the two sensors.

Acknowledgment

The authors would like to thank NASA for funding this research under NRA and GSRP grants. The authors would also like to thankfully acknowledge the several people involved in this project. This includes Dave Hubble and Andy Gifford at Virginia

Tech, Arun Mangalam at Tao Systems, and Larry Hudson at NASA DFRC.

References

- [1] T. E. Diller, Heat flux, in: J. G. Webster (Ed.), *The Measurement, Instrumentation, and Sensors Handbook*, CRC Press, Boca Raton, FL, 1999, Ch. 34, pp. 34.1–15.
- [2] Standard test method for measuring heat flux using flush-mounted insert temperature-gradient gages, DOI: 10.1520/E2683-09, ASTM International, West Conshohocken, PA, 2009, www.astm.org (ASTM Standard E2683, 2009).
- [3] Standard test method for measuring heat flux using surface-mounted one-dimensional flat gages, DOI: 10.1520/E2684-09, ASTM International, West Conshohocken, PA, 2009, www.astm.org (ASTM Standard E2684, 2009).
- [4] A. R. Gifford, D. O. Hubble, C. A. Pullins, T. E. Diller, S. T. Huxtable, A durable heat flux sensor for extreme temperature and heat flux environments, *AIAA J. Thermophysics and Heat Transfer* 24 (1) (2010) 69–76.
- [5] F. P. Incropera, D. P. DeWitt, *Fundamentals of Heat and Mass Transfer*, 5th Edition, John Wiley and Sons, Inc., Hoboken, NJ, 2002, pp. 91–93, 814–815, 907, 929.
- [6] Y. S. Touloukian, Thermal conductivity: metallic elements and alloys, Vol. 1 of *Thermophysical properties of matter*, IFI/Plenum, New York, 1970, pp. 698–699, 1015–1016.
- [7] W. D. Kingery, H. K. Bowen, D. R. Uhlmann, *Introduction to Ceramics*, 2nd Edition, John Wiley, New York, 1976, pp. 634–636.
- [8] R. G. Munro, Evaluated material properties for a sintered alpha-alumina, *J. American Ceramic Society* 80 (8) (1997) 1919–1928.
- [9] N. P. Bansal, D. Zhu, Thermal conductivity of zirconia-alumina composites, *Ceramics International* 31 (2005) 911–916.
- [10] M. C. Croarkin, W. F. Guthrie, G. W. Burns, M. Kaeser, G. F. Strouse, Temperature-electromotive force reference functions and tables for the letter-designated thermocouple types based on the ITS-90, NIST monograph 175, National Institute of Standards and Technology (1993).
- [11] S. Schneider, J. Straub, Laminar natural convection in a cylindrical enclosure with different end temperatures, *Int. J. Heat Mass Transfer* 35 (2) (1992) 545–557.
- [12] V. Kurian, M. N. Varma, A. Kannan, Numerical studies on laminar natural convection inside inclined cylinders of unity aspect ratio, *Int. J. Heat Mass Transfer* 52 (2009) 822–838.
- [13] R. Siegel, J. R. Howell, *Thermal Radiation Heat Transfer*, 4th Edition, Taylor and Francis, New York, NY, 2002, pp. 128, 218.
- [14] B. N. Taylor, C. E. Kuyatt, Guidelines for evaluating and expressing the uncertainty of NIST measurement results, NIST technical note 1297, National Institute of Standards and Technology (1994).
- [15] R. S. Figliola, D. E. Beasley, *Theory and Design for Mechanical Measurements*, 3rd Edition, John Wiley and Sons, Inc., Hoboken, NJ, 2000, pp. 161–163.